Short Wavelength Laboratory Sources

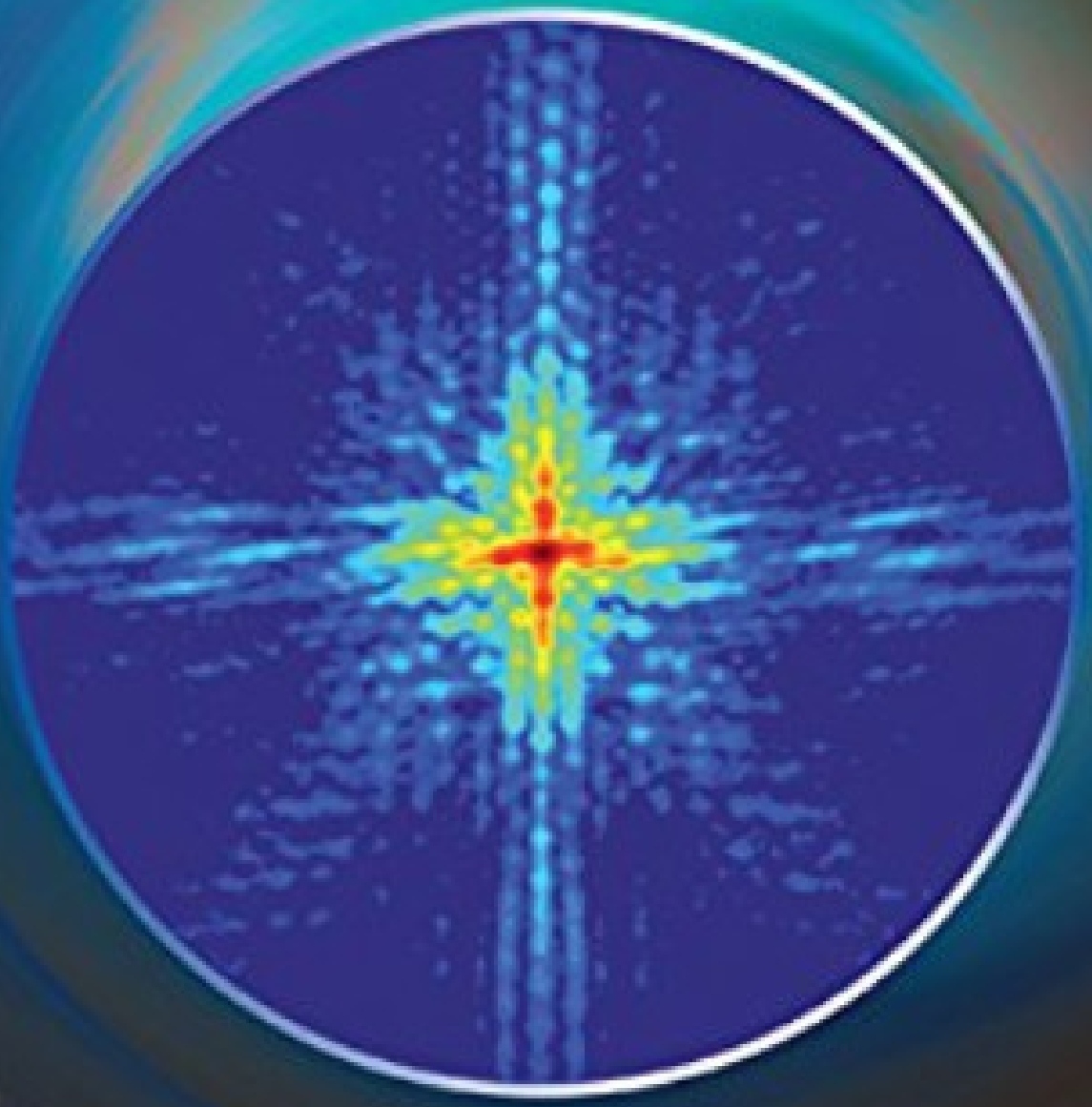

Edited by
Davide Bleiner, John Costello, Francoise De Dortan, Gerry O'Sullivan, Ladislav Pina, and Alan Michette

ROYAL SOCIETY OF CHEMISTRY

cost
EUROPEAN COOPERATION IN SCIENCE AND TECHNOLOGY

ENEA Extreme Ultraviolet Lithography Micro-Exposure Tool: main features

S. Bollanti, P. Di Lazzaro, F. Flora, L. Mezi, D. Murra, A. Torre[a]
ENEA UTAPRAD, via E. Fermi 45, 00044 Frascati (Rome), Italy

The laboratory-scale Micro-Exposure Tool (MET) for Extreme Ultraviolet projection Lithography (EUVL), realised at the Frascati ENEA Centre within the context of a National Project, was successfully operated in 2008 by achieving a 160-nm resolution imaging of mask patterns onto a polymethylmethacrylate (PMMA) photoresist through 14.4-nm radiation (EPL **84**, 58003 (2008)). The MET uses a laser-produced plasma as EUV radiation source, a couple of twin ellipsoidal mirrors as collecting optics to gather the 14.4-nm radiation from the source to the mask, an efficient combination of ambient gas and mechanical device as debris mitigation system (DMS) and finally a low-cost Schwarzschild objective (SO) as projection optics to image the patterned mask onto the wafer. The paper gives details of the ENEA MET components and of the aforementioned successful operation along with subsequent related investigations.

Keywords: Extreme ultraviolet lithography, Laser-produced plasma source, Debris mitigation system, Schwarzschild objective, Micro-Exposure Tool, Nanopatterning
PACS: 02.30.Gp; 45.25.-p

1. Introduction

In [1, 2] the successful operation of the laboratory-scale EUVL MET, realised at the ENEA Frascati Research Centre in the frame of an Italian National Project [3], was reported, describing the achieved high-resolution patterning on a PMMA photoresist.

EUV (λ = 10-15 nm) lithography has come a long way in the last 25 years [4]. The idea of EUVL as a possible extension of the conventional optical lithography traces back in fact to 1985 [5], whereas the first experimental results, showing the possibility of resolving 0.5-μm structures using a Schwarzschild objective as the projection (demagnifying) optics, synchrotron radiation as the source and a reflective-type mask, were reported in 1989 [6][1]. Such a result is to be compared with the recent achievement by AMSL, whose NXE:3100 tool has printed lines and spaces of 18 nm [7].

A survey of more than 130 attendees at the 2010 SEMATECH Litho Forum [8] confirmed the general trend, emerged as well at previous such forums, to continue lithography's current course being considered the best way to manufacture next-generation chips. Indeed, 193-nm immersion double patterning continues to be considered the suitable lithographic technology for volume manufacturing in 2012 at the 32-nm half-pitch node, whilst EUVL stands out as the only candidate for semiconductor manufacturing at the 22, 16 and 11-nm half-pitch nodes. Its placing into manufacturing is expected in 2014, with EUV extension being the technology of choice for

[a] Corresponding author. Email: amalia.torre@enea.it

[1] The work was presented at the 33rd International Symposium on Electron, Ion, and Photon Beams, Monterey, California, May 30-Jun. 2 (1989). In this regard, in the EUVL historical perspective, addressed to in [4] (Chapter I, by Kinoshita and Wood), one can read: "At the EIPB symposium banquet..., a Russian scientist, Dr. Tanya Jewell of AT&T, cornered Dr. Kinoshita and proceeded to deluge him with questions. The combination of poor Japanese English and poor Russian English made conversation extremely difficult, so the discussion continued for a long time with Obert Wood of AT&T acting as interpreter. The following year, AT&T announced the printing of 0.05-μm patterns using SXPL. The authors of this chapter regard the discussion that night in Monterey in 1989 as having been "the dawn of EUVL"."

2016. Several, however, are the EUV technology challenges; in particular, source power, mask defects, exposure tool throughput, and cost of ownership are rated at the top of the list.

Discharge-produced plasma and laser-produced plasma (LPP) are the leading technologies for generating high-power EUV radiation. In both technologies, hot plasma of $\sim$ 20-50 eV of the chosen fuel material is generated, which produces EUV radiation. Xenon, tin and lithium are the fuel materials of choice for EUV sources [6, 9]. Radiation at 13.5 nm is currently explored for printing. Yet, the ever increasing resolution demand of the semiconductor industry prescribes that future lithography equipment operates at an even shorter wavelength (6.X nm), i.e. beyond the EUV range (BEUV) [10].

The radiation emitted by the plasma, possibly debris-cleaned by an appropriate DMS, is gathered by the collector optics and focused to the intermediate focus (IF), from where it is relayed to the scanner optics and finally to the wafer. It is at the IF that the source specifications are settled in accord with the high-volume manufacturing requirements, so that the appropriate exposure tool, and particularly its illuminator, does not depend on the EUV source features.

LPP sources seem to offer the most promising technology to reach the power levels needed for high-volume manufacturing. Indeed, the requirements for source power have increased over time as it has become clear that high resist dose is needed to simultaneously meet resolution and linewidth-roughness targets. Thus, it is estimated that for the 22-nm half-pitch generation an EUV power $\sim$ 400 W at the IF within a 2% bandwidth window around the standard exposure wavelength for EUVL is required for 10-mJ/cm^2 photoresist sensitivity to enable $>$ 100 wafer per hour scanner throughput.

Several are the proposed and implemented methods to control and/or mitigate the source-emitted debris with the intent of protecting the collector mirror, one of the most costly element in a EUVL setup. DMSs based on the use of ambient gas for moderating the species [11, 12] (also combined with a protective covering over the collecting optics [13]), or of foil traps for particle capture [14] as well as on the application of electric [15] and/or magnetic fields [16] for deflection or velocity reduction (also combined with an ambient gas [17]) are well documented in the literature, with the specific DMS structure being devised and optimized according to the EUV source of concern [18, 19].

The DMS, implemented in the ENEA MET, combines Krypton as ambient gas at a suitable pressure with a gas filter and a specifically designed fan. It effectively cleans the $\lambda > 13.8$ nm Kr-penetrating radiation, which is firstly collected by one of the two twin ellipsoidal mirrors to the IF and then redirected by the other mirror to the reflective mask through further two Mo/Si multilayer mirrors. Finally, a SO is the projection (demagnifying) optics, deputed to replicate the patterned mask onto the wafer (Fig. 1.1).

The main features of the ENEA MET components are synthesized in Sect. 2. Indeed, following the radiation path, we will highlight the characteristics of the source, the DMS, the collector, the mask illuminating mirrors, and the imaging optics. Emphasis will be put on the latter, the SO design, mounting and alignment being described in detail. Section 3 gives an account of the successful operation of the device, reported in [1], and of the SO transmission measurement, subsequently carried out in order to identify the cause of the unexpectedly poor performance (as to the overall reflectivity, indeed) of the objective. Concluding notes are given in Sect. 4.

2. ENEA MET: setup

Figure 2.1 shows the top view of the EUV lithographic setup of the ENEA MET, displaying the source, the collector and the printer modules. These are suitably embedded into two vacuum chambers, which are connected through a flexible duct. One chamber contains the source, the col-

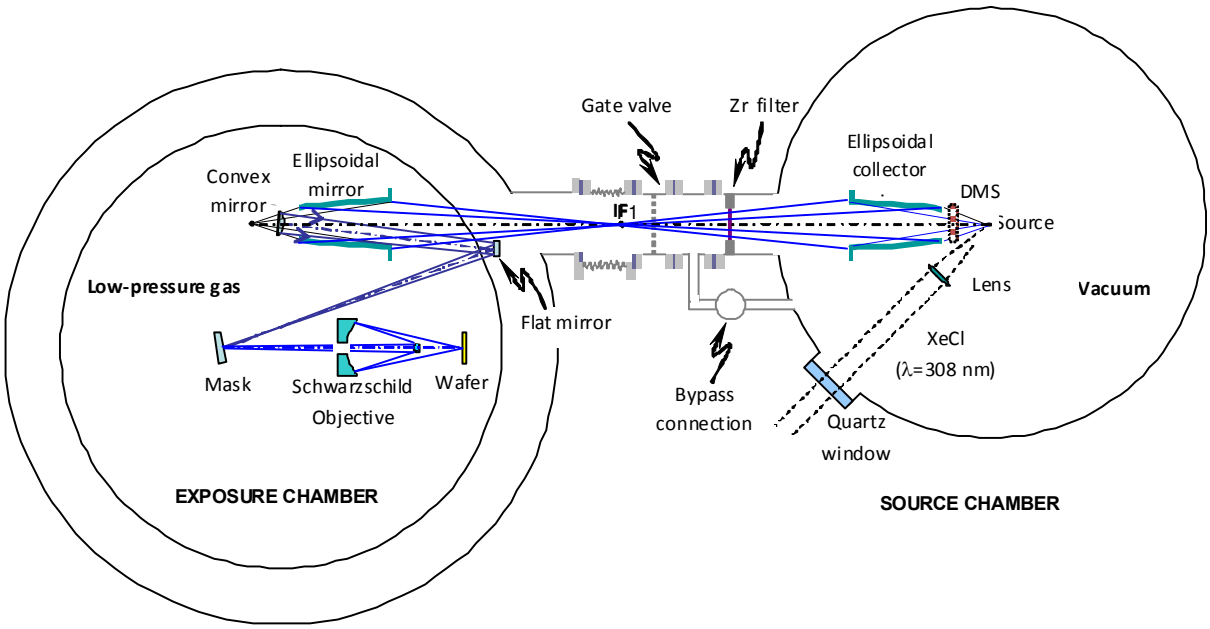

Figure 1.1: Layout of the ENEA EUVL MET, which uses a laser-produced plasma as a radiation source, a couple of twin ellipsoidal mirrors as collecting optics to gather the 14.4-nm radiation from the source eventually to the mask, an efficient combination of ambient gas and mechanical fan as DMS and finally a low-cost SO as projection optics to image the patterned mask onto the wafer.

lector and the DMS, whilst the other the illumination and projection optics. All the illumination and projection optics lie on a vibration isolated and temperature controlled Invar board.

2.1. Source module

The ENEA MET exploits the LPP solid-tape-target source of the EGERIA (Extreme ultraviolet-radiation Generation for Experimental Research and Industrial Applications) facility, which emits over a wide and fairly tunable range from ~ 40 eV to ~ 2 keV.

Characteristics and performances of the EGERIA source, which presents unique features among similar sources as regards the pulse energy and duration, are detailed in a number of papers [12, 20, 21]. Here, we briefly recall that the characteristics of the emitted radiation such as spectral range and purity, peak intensity, pulse width, and conversion efficiency can be controlled by the intensity, pulse duration and repetition rate of the drive laser and by the target material. The source can alternatively be driven by two different high peak-power high repetition-rate XeCl lasers ($\lambda = 308$ nm); precisely, the laser facility Hercules (developed by ENEA Frascati) whose pulse energy, width and repetition rate are respectively $E_L = 6$ J, $\tau_L = 120$ ns and $p.r.r. \leq 5$ Hz and the commercial Lambda-Physik LPX-305 laser having $E_L = 0.5$ J, $\tau_L = 30$ ns and $p.r.r. \leq 50$ Hz. Target materials such as Sn, Cu, Ta and In are available for different applications and/or investigations as well as operating wavelength. For instance, Sn and In are appropriate for lithographic processing at respectively $\lambda = 13.5$ nm and $\lambda = 14.4$ nm. The choice for the drive laser is dictated by whether a high energy per pulse or a high number of laser shots is required. In any case, emission in the EUV spectral range, which is basically favoured by a long laser pulse width, is further optimized by a proper out-of-focus condition of the laser beam.

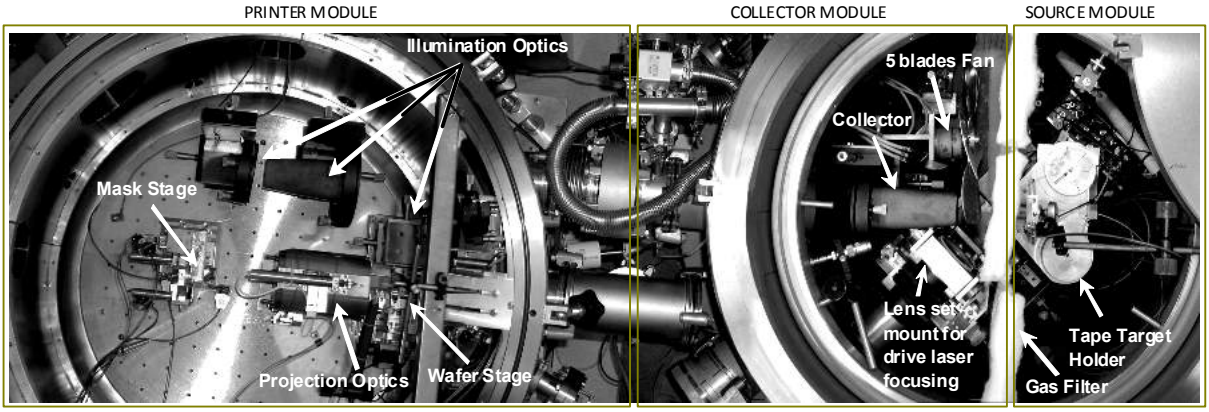

Figure 2.1: Top-view of the ENEA MET, showing the two vacuum chambers; one chamber contains the plasma source, the collector and the DMS, whilst the other chamber houses the illumination and the projection optics.

In fact, as can be seen in Fig. 2.2, by moving the target out of the focus of the 12-cm focal length triplet lens, one can "tune" the emission spectral range as the laser irradiance is made to vary from keVs (at the focal position) to tenths of keVs. Specifically, at about 2 mm away from the focus, the laser irradiance is $I_L = 10^{10}$ W/cm^2, by which EGERIA is made to convey EUV radiation in a beam with a half-power beam width of tenths of mm and with a relevant conversion efficiency up to $\sim 0.7\%$ per eV over the 2π solid angle. Moreover, when defocusing the laser beam, the laser irradiance is very less sensitive to both fluctuations of the target position, and laser energy/divergence instabilities, thus yielding a very good shot-to-shot stability.

2.2. Collector module

The radiation pulse, after being debris-cleaned by the patented DMS, sequentially hits a pair of identical ellipsoidal mirrors, which serve to gather the emitted radiation and to transport it from the source to the projection chamber (Fig. 1.1).

2.2.1. Debris Mitigation System

Debris in a solid-type LPP source include energetic ions, neutrals and particulates. Of course, atomic and particulate debris behave differently; hence, an efficient DMS must embed different tools to effectively affect both kinds of debris.

An accurate speed-size characterization of atomic and particulate debris, emitted by the EGERIA source, has been performed [22, 23]. Also, the mitigating efficiency of various tools, i.e. ambient gas (Ar and Kr), mechanical interdicting device (fans with different numbers of blades and speeds) and magnetic field, has been tested by observing the plasma debris contamination of glass slides, exposed - under different enviromental conditions and laser shot numbers - to the radiation from a Cu tape, irradiated by the Lambda-Physik laser.

As a result of such analyses, the ENEA MET DMS was designed to combine an ambient gas with a fan, further supported by a gas filter for continuous gas cleaning (Fig. 2.1). The ambient gas, specifically Kr at a pressure ≤ 1 mbar such to allow for a $\sim 86\%$ EUV transmission through the overall target-to-collector distance (~ 75 mm), serves to slow down and possibly block the debris of small/moderate sizes, i.e. with diameters up to 1 μm, mostly the atomic component

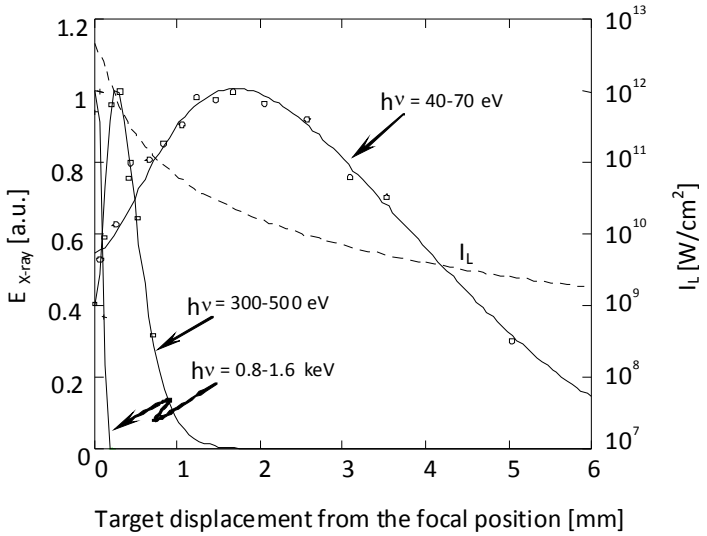

Figure 2.2: EGERIA-pulse energy in different spectral intervals and laser irradiance on the target (dashed line) vs. target position behind the focal plane for a 100-μm thick Cu tape target irradiated by Hercules laser pulses [12,20].

(neutrals and ions). The fan is in turn aimed at interdicting the arrival on the collector of the particulates which, due to their quite varied sizes (i.e. diameters $\sim$ 1-10 μm) and the mechanism of their formation, are scarcely moderated by the gas, but have velocities significantly smaller than those of the atomic debris. Specifically, the 5-blades alluminum alloy fan, shown in Fig. 2.1, were in use during the aforementioned successful operation of the MET. It has a maximum angular velocity $\omega_{max} = 400\pi$ Hz, and is placed at a minimum distance of 4 cm from the source.

The use of Kr (atomic weight = 84 amu) is preferred with respect to Ar (atomic weight = 40 amu), since, as it emerges from both theoretical estimates and experimental tests [12, 22–24], the mitigating power of Kr is definitely higher than that of Ar under comparable operating conditions, involving also larger ranges of both debris sizes and speeds. However, since Kr unefficiently transmits the EUV radiation up to 13.8 nm, at which it becomes well transparent, the use of a Kr-based DMS requires to shift the operating wavelength of the lithographic setup from the standard 13.5 nm to values $>$ 13.8 nm. Notably, over the wavelength range 14-14.5 nm the typical Mo/Si multi-layer EUV mirrors maintain the same spectrally integrated reflectivity also after the multiple reflections occurring along the radiation path from the source to the wafer [22].

Observation of the debris-flux exposed glass plates by both the optical microscope and the microdensitometer resulted in very encouraging values of the debris mitigation factor (DMF) for both atomic and particulate debris [22]. In particular, values up to 450 for the DMF relatively to atomic debris were deduced from the optical density measurements by a microdensitometer. As described in detail in [24] and also summarized in [23], the analysis of the exposed glass-slides in relation to the particulate debris (i.e. clusters and droplets with diameters $\gtrsim 10^{-3}$ μm), performed by a code specifically developed for the associated slide-image processing, has confirmed the effectiveness of the DMS. The code, which resorts to some basic image processing routines of the inherent MATLAB toolbox (V5.4) [25], relies on specific procedures, built on the basis of an accurate observation of the various images, for debris recognition, spot fine-structure identification and debris size (both above and below the microscope resolution) evaluation [24]. Indeed, the rather good performance of the DMS has allowed quite a safe operation of the ENEA

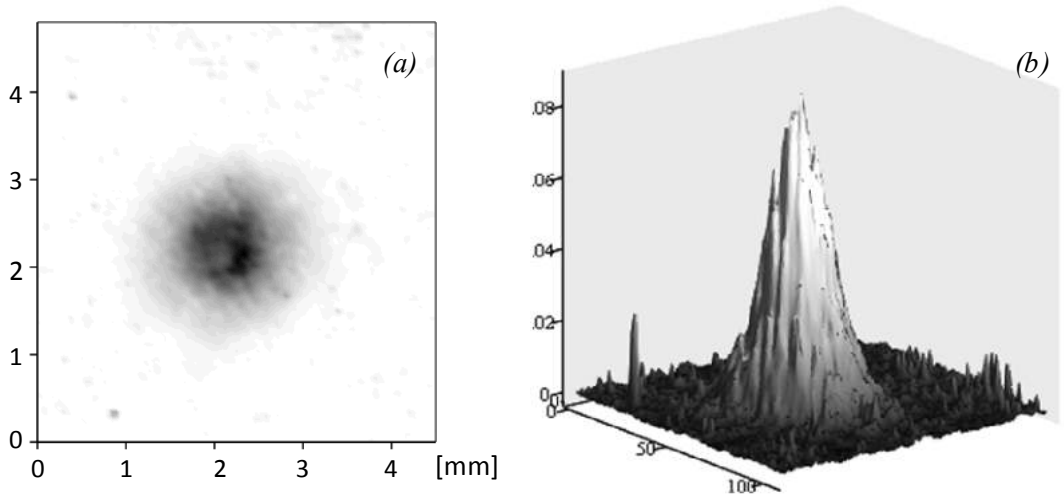

Figure 2.3: *(a)* Image and *(b)* surface plot of the optical density spatial distribution induced by the properly filtered EUV radiation from EGERIA source on a dosimetry film at the IF [1].

MET with the achievement of a 160-nm resolution patterns from a multi-layered mask on a PMMA photoresist, although a much higher number of laser shots was unexpectedly required [1].

2.2.2. Collector optics

The two ellipsoidal grazing-incidence Ru-coated mirrors have been made by Media Lario Technologies (Italy) [26]. Their symmetrical configuration is aimed at maintaining the homogeneity of the source angular distribution at the focus of the second mirror. The first ellipsoidal mirror is placed in the source chamber (Fig. 2.1). It collects the radiation from the source, emitted between 9° and 19° with respect to the target normal, and redirects it to the IF with an effciency $\geq 8\%$ (over a 2π solid angle) and an integrated reflectivity of $\sim$80% in the EUV. Actually, before reaching the IF, the radiation is spectrally filtered by a 50%-EUV-transmittance, 150-nm thick, Ni-mesh supported Zr filter (Luxel Corporation, USA), which blocks most of the out-of-band radiation and also isolates the 1mbar Kr-gas in the source chamber from the 10^{-6}-mbar vacuum in the projection chamber.

Figure 2.3 shows the spatial distribution at the IF of the 0.8-μm-Al-foil filtered radiation, as measured by the optical density variation induced on a Gafchromic HD-810 Radiochromic Dosimetry film. The relationship between EUV intensity and optical density is almost linear in the explored range [1].

2.3. Printer module

The second ellipsoidal mirror is placed in the projection (and exposure) chamber. It conveys the filtered radiation gathered from the IF to the mask illuminating optics (Fig. 1.1). As such, it can be considered as a component of the printer module, whose central part is indeed the Schwarzschild objective, by which the pattern reflected by the mask is eventually imaged on the wafer.

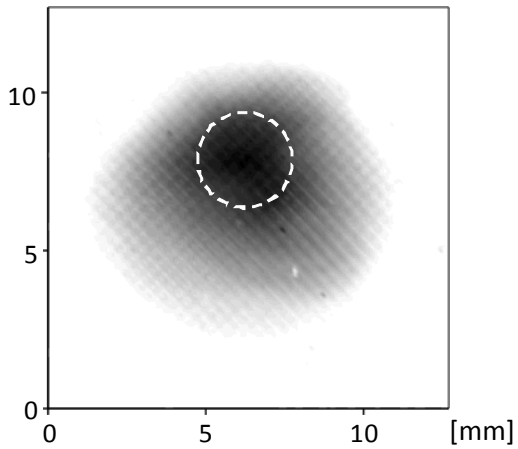

Figure 2.4: Image of the optical density spatial distribution induced by the properly filtered EUV radiation from EGERIA source on a Q-plate at the mask plane. The dashed circle highlights the high-resolution object field of the SO [1].

2.3.1. Mask illuminating optics

Two Mo/Si multilayer mirrors, sequentially spherical convex and flat, serve to focus the EUV radiation, conveyed by the second ellipsoidal mirror, on the patterned mask. Both mirrors along with the Mo/Si mask were made by the INFN Legnaro Laboratories (Italy) [27] with up to 65% reflectivity peak at the operating conditions, as tested at the BEAR beam-line of ELETTRA in Trieste (Italy) [28], whereas the absorbing patterns on the mask were made by CNR-IFN in Rome [29]. Thanks to the high convex-mirror magnification and to the suitable compensation of the convex-mirror spherical aberration by a slight longitudinal shift of the second ellipsoidal mirror from the relevant confocal position, the mask comes to be nearly homogeneously illuminated over a 3-mm-size area as shown by the image in Fig. 2.4. This fits well with the high-resolution projection field dimension of the SO, evidenced by the dashed circle in the figure. The image has been obtained exposing at the mask plane an Ilford Q-plate to the incoming radiation; the shadow of the Ni-mesh wires supporting the Zr filter is clearly distinguishible in the figure. The EUV energy density (fluence) on the mask has been measured by an IRD photodiode model AXUV20BNC and results to be $\sim 10\ \mu\mathrm{J/cm^2/shot}$ [1].

2.3.2. Mask imaging optics

The optical system, specifically designated to transfer the desired pattern from the illuminated mask on the semiconductor wafer, is of preminent relevance within the context of the EUVL. SO-based configurations have been proved to be good condidates for such an issue. The SO is a convex-concave mirror system, in which the mirrors are concentric [30]. Accordingly, it conveys the simplest optical scheme that can be devised as an effective projection system for EUVL, when configured as a reductor, i.e. with the illumination field from the object hitting firstly the convex and then the concave mirror, as exemplified in Fig. 2.5.

The SO is characterized by the object-to-image formula,

$$V(t,\alpha) = t\frac{\sin\alpha}{\sin\alpha'}, \tag{2.1}$$

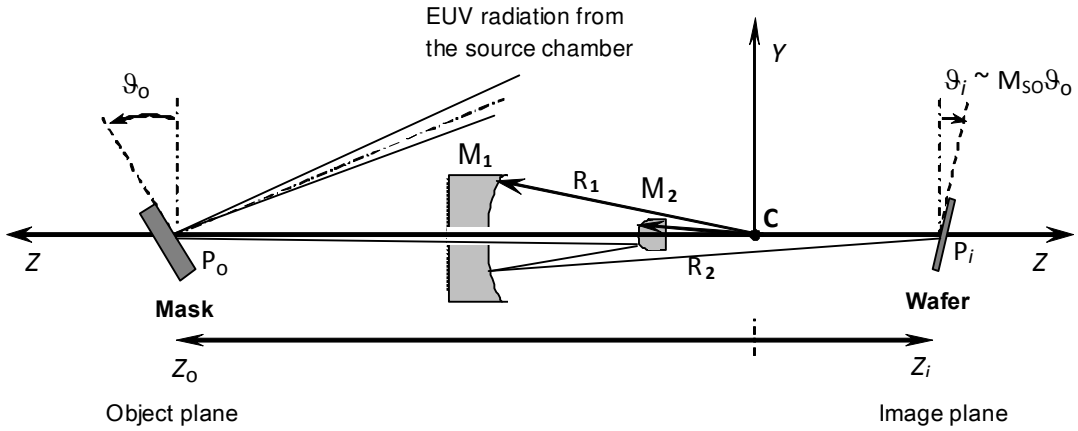

Figure 2.5: Typical arrangement of a SO-type reductor in an EUVL imaging setup, showing the mask (i.e. object) plane and the wafer (i.e. image) plane. (**C** = common centre of curvature of the two SO mirrors)

where V and t denote the axial positions Z_o and Z_i of the on-axis object and image points (in the respective object and image space) scaled to the curvature radius of the convex mirror, i.e. $V \equiv \frac{Z_i}{R_2}$ and $t \equiv \frac{Z_o}{R_2}$, whereas α and α' are the inclination angles to the optical axis of the incoming and emerging ray. The latter are related by

$$\alpha'(t,\alpha) = 2\sin^{-1}(t\sin\alpha) - 2\sin^{-1}(\frac{t}{r}\sin\alpha) - \alpha, \tag{2.2}$$

with r addressing the concave-to-convex mirror curvature radii ratio: $r = \frac{R_1}{R_2}$.

The "standard" SO configuration provides an easily feasible system, and so convenient as regards manageability, costs and alignment issues in comparison with multi-elements projection optics. Also, it is capable of yielding the high resolutions required by the EUV lithography, albeit over a rather limited exposure field.

ENEA MET SO: design As a basic characterization, the ENEA MET SO has been designed to have an image-space numerical aperture $NA = 0.23$, a magnification $M \sim 1/9.7$, mirror curvature radii $R_1 = 144.23$ mm and $R_2 = 45.06$ mm, and respective mirror diameters $\Phi_1 = 74$ mm and $\Phi_2 = 12.7$ mm. It has been manufactured by Société Européenne de Systèmes Optiques (SESO, France) [31], with a global figure error ≤ 8 nm, and an expected reflectivity-curve peak $\geq 65\%$ at 14.4 nm over the whole coated surfaces of both mirrors (by a graded multilayer coating).

More precisely, the configuration implemented in the ENEA MET is the so-called modified SO (MSO) configuration [32]. It preserves the mirror concentricity of the standard configuration[2] while optimizing the SO performance toward a better resolution by placing the mask and the wafer at suitably designed locations, different from those conforming to the standard configuration [34, 35]. Specifically, in the ENEA MET SO the mask and wafer axial positions Z_o and Z_i are respectively $Z_o = 340.22$ mm and $Z_i = 36.26$ mm, whereas the values corresponding to the standard configurations would be $Z_o = 350.296$ mm and $Z_i = 36.138$ mm.

[2]Let us recall that, in view of extending the good performance characterisitcs of the SO to a larger exposure field, further schemes have been proposed. For instance, in the SO-based configuration, analysed in [33], the mirrors are slightly displaced from the concentric location while the object and image planes are correspondingly placed at positions such to vanish, as in the ordinary SO, the third-order longitudinal aberrations.

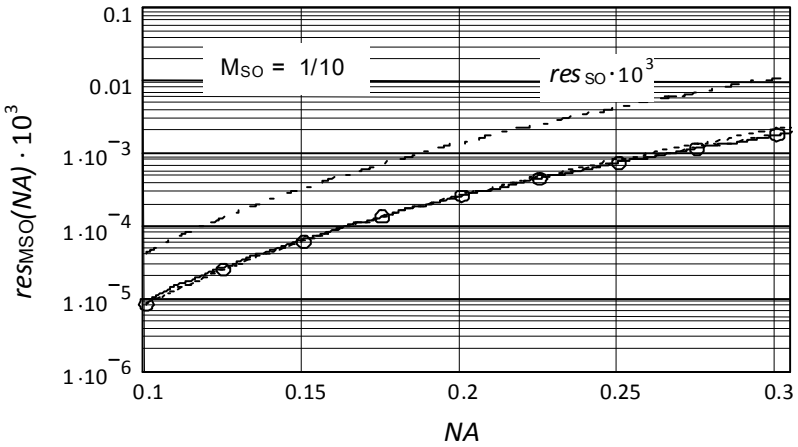

Figure 2.6: R_2-scaled geometrical resolution vs. NA in a MSO for $M_{SO} = 1/10$, as conveyed by simulations based on the ZEMAX code (o's) and on specific analytical expressions(dashed lines). The solid line reproduces the relevant best fit (2.3), the corresponding curve for a SO being also shown (dot-dashed line) [34].

A detailed analysis of the properties of the MSO configuration, as regards, for instance, the dependence of the image-plane resolution and third-order aberrations on the numerical aperture and on-axis object position has been presented in [34, 35]. It was shown there that the typical worsening trend of the geometrical resolution in a conventional SO configuration with increasing the numerical aperture is significantly mitigated (by a factor ~ 5 for the magnification of concern) in the corresponding modified scheme. In fact, as conveyed by Fig. 2.6, the resolution vs. numerical aperture curve in a MSO lies markedly below that pertaining to the ordinary SO.

In conformity to the spirit of the quoted references, the figure reports the results of both a semi-analytical procedure and a numerical simulation. The former resorts to analytical expressions for the geometrical resolution RES, defined as the standard deviation of the off-axis distances of the image points over the image plane, which have been numerically elaborated by the Mathcad 13 package, whereas the latter directly conveys the rms radius of the ray distributions around the chief ray, resulting from the sequential ray-tracing performed by the lens-design ZEMAX code [36]. Moreover, the ZEMAX-conveyed values are synthesized through best fit procedures into compact scaling laws of the system design parameters vs. the numerical aperture. Thus, the R_2-scaled geometrical resolution $res \equiv \frac{Res}{R_2}$ in the SO and MSO schemes is ruled as

$$res_{SO}(NA) = 4.71 \cdot 10^{-3} NA^{5.07}, \quad res_{MSO}(NA) = 1.17 \cdot 10^{-3} NA^{5.2}, \tag{2.3}$$

over the examined range of values $NA = 0.1 \div 0.3$, and $M_{SO} = 1/10$. Here, M signifies the paraxial magnification relative to an assigned object plane, defined as usual by the ratio of the paraxial image position over the corresponding object position, and hence in a SO it is given by

$$M_{SO}(t, r) = \left.\frac{V(t, \alpha)}{t}\right|_{\alpha \to 0} = \frac{r}{2rt - 2t - r} = \frac{r - 1 + \sqrt{r}}{r - 1 - \sqrt{r}}. \tag{2.4}$$

As said, in the ENEA MET SO $M \sim 1/9.7$

However, the advantage of the improvement of the geometrical resolution is contrasted by the corresponding reduction of the depth of focus. Therefore, the choice for a specific configuration to implement turns out to be a matter of a convenient compromise [37].

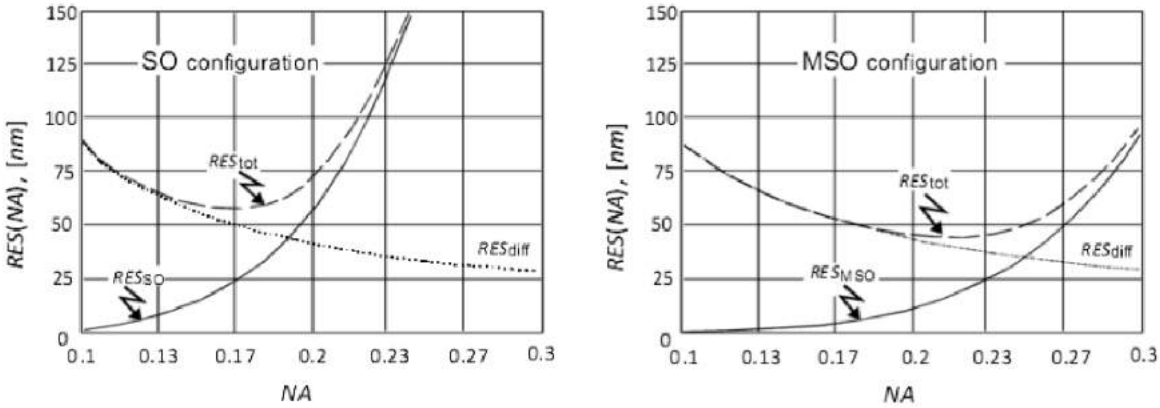

Figure 2.7: Spatial resolution vs. NA in a standard and a modified SO configuration, in the case of $M_{\text{SO}} = 1/9.69$, $R_2 = 45.06$ mm and $\lambda = 14.4$ nm [37].

EUV imaging cannot use refractive optical elements and hence entirely reflective optical components must be used. Therefore, in an EUV lithographic setup the mask is rotated with respect to the optical axis, thus resulting into a degradation of the resolution on the wafer. However, as expected according to the Scheimpflug principle [38], this effect can effectively be contrasted by a reciprocal tilt of the wafer. The analysis presented in [35] has in fact confirmed that by a symmetrical suitable tilt of the wafer (Fig. 2.5) the performance of the untilted-mask device can be restored as regards the values and the resolution distribution across the optical axis in the wafer plane. The paraxial magnification roughly rules the ratio between the tilts of the image and object plane, so that, in the ENEA MET SO, the $\vartheta_o = 10^\circ$ tilt of the mask with respect to the optical axis is compensated by the symmetrical $\vartheta_i \sim M_{\text{SO(MSO)}}\,\vartheta_o \sim 0.1^\circ$ tilt of the wafer.

ENEA MET SO: mounting and alignment The above consideration has been concerned only with the geometrical resolution. Actually, the spatial resolution comprises also the diffraction-limited resolution res_{diff} according to

$$res_{\text{tot}} = \sqrt{res^2_{\text{SO(MSO)}} + res^2_{\text{diff}}}, \tag{2.5}$$

where the R_2-scaled diffraction limited resolution $res_{\text{diff}} \equiv RES_{\text{diff}}/R_2$ is well known to vary inversely with NA, since

$$RES_{\text{diff}}(NA) = 0.61\frac{\lambda}{NA}. \tag{2.6}$$

The two contributions entering (2.5) are plotted in Fig. 2.7 for both the standard and the modified configurations in correspondence with the specific values $M_{\text{SO}} = 1/9.69$, $R_2 = 45.06$ mm and $\lambda = 14.4$ nm pertaining to the ENEA MET SO setup. Whilst in the standard configuration the geometrical resolution dominates the system performance at relatively small numerical apertures, $NA \geq 0.15$, in the modified configuration the geometrical resolution becomes predominant over the diffraction limited resolution only at larger numerical apertures, $NA \geq 0.25$. Accordingly, the choice of the design parameters for the ENEA MET SO setup has been dictated by a reasonable compromise between easy system manageability and resolution request down to 50 nm. Indeed, the geometrical resolution was expected to be $RES_{\text{MSO}} \sim 27$ nm for the designed

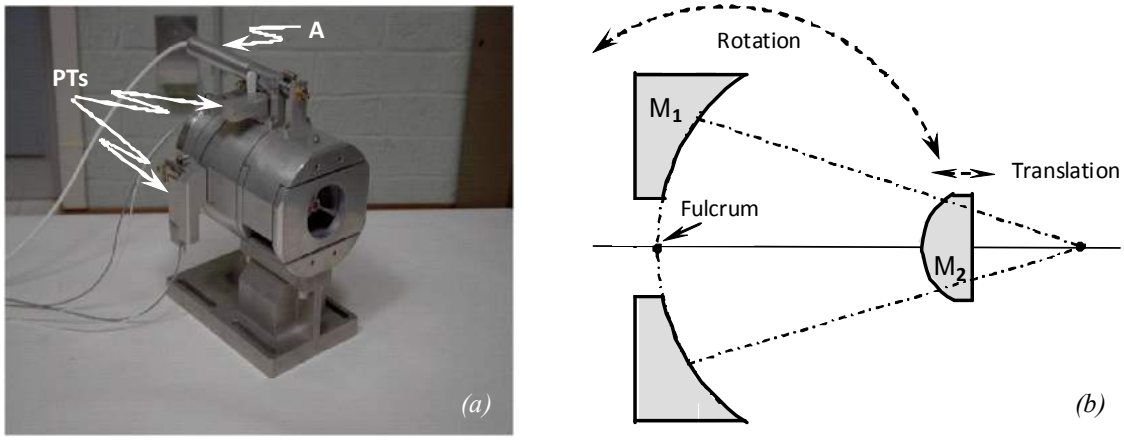

Figure 2.8: *(a)* SO mounting-block in the ENEA MET: the two piezoelectric transducers (PT) and the actuator (A) are clearly visible; *(b)* Schematic of the mirrors control; the coincidence of the concave mirror rotation fulcrum with its vertex enables the steadiness of the two-mirror distance during tilting.

MSO configuration, whilst $RES_{\text{diff}} = 38$ nm, thus yielding $RES_{\text{tot}} \sim 47$ nm as the best resolution one could expect in the designed setup.

Evidently, in view of approaching such a value as close as possible, the alignment of the SO mirrors becomes crucial on account as well of the rather severe tolerance on the perfect mirror concentricity. In fact, by proper ZEMAX ray-tracing simulations, aimed at analysing the dependence of the geometrical resolution on the two-mirror decentring, such a tolerance (defined as the distance between the centres of curvature of the two mirrors which causes a $\sqrt{2}$ worsening in the resolution) has been estimated to be of $\sim$10 μm and $\sim$1 μm for decentring respectively along the z-axis and in the transverse plane.

In this connection, the mechanical mounting of the objective is of specific relevance as to movement precision (repeatability in positioning) and stability. In Fig. 2.8a the SO mounting-block is shown. It consists of a cylinder made by a single piece of aluminium alloy with special thinned sections allowing for three degrees of freedom. The first two enabled movements are rotations of the concave mirror (which is located at the back end of the mount cylinder in the picture) around two mutually orthogonal axes with an angular resolution of ~ 2 μrad. Both axes are orthogonal to the optical axis, and cross each other at the mirror vertex. The rotations are controlled by piezoelectric transducers (Physik Instrumente, model P-601.3SL), visible in the picture. As a third degree of freedom, the translation of the convex mirror (located at the centre of the parallelogram structure recognizable at the front end of the mount cylinder in the picture) along the optical axis is allowed, being controlled by an actuator (Physik Instrumente, model M-227.10) with a ~ 0.1 μm longitudinal resolution. The scheme in Fig. 2.8b should clarify the "dynamics" of the SO mirror movements.

The SO alignment has been carried out by exploiting the well known Foucault technique [39], whose validity has already been demonstrated in the EUV for a SO [40–43]. However, since the in-band EUV power at the wafer level in the ENEA MET was unexpectedly too low to allow for an at-wavelength alignment in a reasonable time, the Foucault test-based SO alignment has been performed by using ultraviolet light and overcoming the inherent limitations (related to the diffraction limit of the alignment wavelength) through a novel procedure, briefly addressed

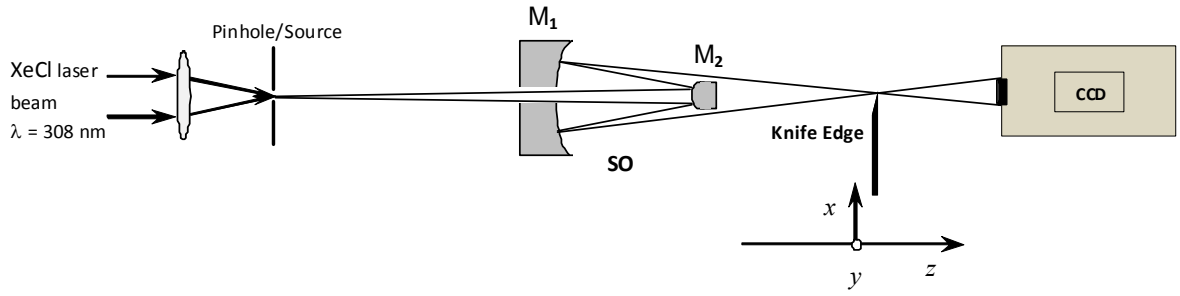

Figure 2.9: Schematic (not in scale) of the experimental setup for the SO alignment by means of the revised Foucault-test based technique, described in the text.

to in [2] while described in detail in [44]. Quite in general, an at-wavelength alignment on low-power laboratory plasma source is time expensive and component consuming. Therefore, the proposed alternative technique can conveniently be exploited when EUV/soft X-ray sources with a limited photon flux are involved. It is based on an accurate diagnostics for system aberrations (that evidently indicate mirror misalignments), gained from an experimental characterization and a reliable modelling of the dependence of the SO longitudinal aberrations on the mirror misalignments, so that it is possible to individuate the aberration source and accordingly adjust the SO alignment parameters.

The setup of the procedure as implemented in the ENEA MET is sketched in Fig. 2.9: the ultraviolet beam of a XeCl laser ($\lambda = 308$ nm) is focused by a 12.5-cm focal-length triplet lens in a $\sim$50-μm diameter spot on a 5-μm diameter pinhole, which then, being illuminated by the central, quite uniform portion of the Airy disk, provides the on axis point-like object-source for the SO. After the SO, in the "classical" Foucault test the beam would be cut at the focal plane by a knife edge (KE) moving perpendicularly to the optical z-axis; this would generate on the observation plane the typical images, called foucaultgrams, corresponding to different kinds of aberrations, mainly spherical and coma aberrations in the case of the SO. In fact, in the case of the SO, a longitudinal mirror decentring causes a spherical aberration, with marginal and paraxial rays having different focal distances, shorter (longer) for the former according to whether the two mirrors are closer to (farther from) each other relatively to the concentric condition. In turn, a transverse shift of the two centres of curvature produces a coma aberration, witnessed by the typical comet-like figure on and in proximity of the focal plane. Evidently, on account of the afore-described ENEA MET SO mounting, the spherical aberration can be controlled through the longitudinal translation of the convex mirror, whereas the coma aberration by tilting the concave one.

The drawbacks of aligning the SO by using a wavelength much larger ($\sim 20\times$, in our case) than the operating one can in some way be overcome by looking at the sequence of foucaultgrams obtained with a longitudinal scanning of the KE kept at 50% of the beam transmitted power. This has two advantages with respect to the transverse KE scanning in the focal plane: firstly, the longitudinal aberrations extend over a wider spatial scale, increasing the sensitivity to their occurrence; secondly, the transmitted power which reaches the observation plane is almost constant for the different KE positions (that is for each sequence of foucaultgrams).

The foucaultgrams are recorded on the CCD sensor of a 16-bit-dynamics PI-MTE:1300B Princeton Instrument camera, which is put at a distance from the SO focal plane such that

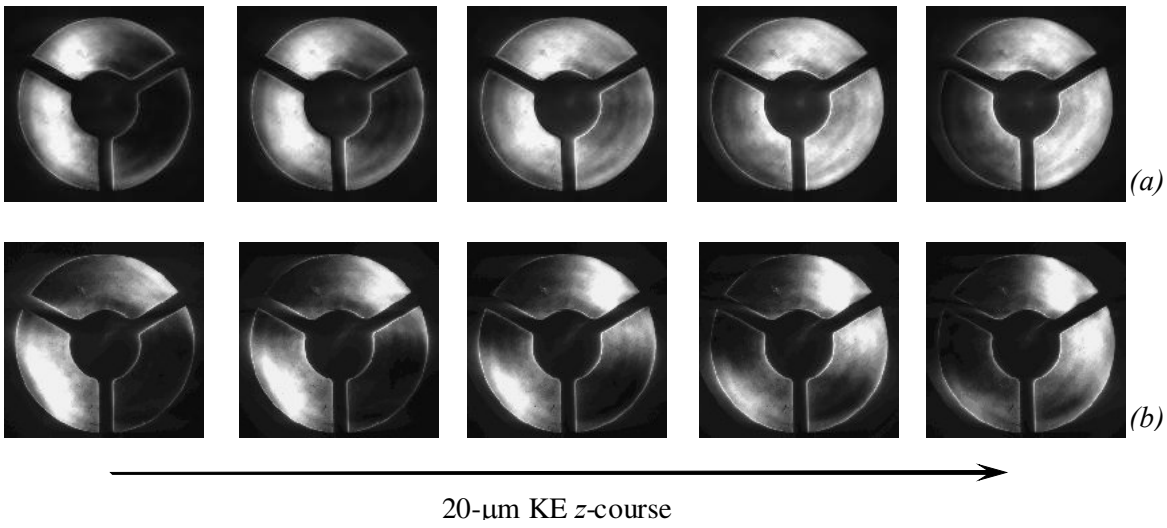

Figure 2.10: Sequences of foucaultgrams of the ENEA MET SO, obtained for a longitudinal KE scan over 20 μm, in correspondence with controlled decentrings of the SO mirrors which induce *(a)* a spherical aberration with the mirrors nearer to each other with respect to the concentric condition of $\sim$350 μm, and *(b)* a coma aberration with the concave mirror tilted by $\sim$ 0.84 mrad, corresponding to a transverse decentring of $\sim$120 μm. In both cases the KE allows the transmission of half the beam power [44].

the 26.8×26.0 mm^2 imaging area be almost completely illuminated. The transverse position of the KE is fixed when the power collected by the CCD is half of the full power (i.e. in absence of the KE) within the range of the KE longitudinal positions of interest. After that, by means of a longitudinal scan of the KE, it is possible to identify the type of the occurring aberration and to evaluate its amount. Exemplificative camera-recorded foucaultgrams are shown in Fig. 2.10. They have been obtained for a longitudinal KE scan over 20 μm, with the KE transverse position being controlled in order to transmit $\sim$ 50% of the power, and clearly reveal the occurrence of spherical and coma aberrations, induced by the controlled decentring of the mirrors, as specified in the caption.

Besides using the ZEMAX code for simulating the SO behaviour, we developed a proprietary Visual C++ ray-tracing program to reproduce the observed foucaultgrams. The program demands as input data the longitudinal distance between the SO mirror centres of curvature and the orthogonal tilts of the concave mirror, along with the KE and CCD positions. For instance, the sequence of camera-recorded foucaultgrams of Fig. 2.10 is paralleled by that in Fig. 2.11, showing the foucaultgrams, conveyed by the program in correspondence with similar mirror decentrings.

Since the knife moving along the z-axis crosses a focal plane, the shadow position on the CCD changes from right to left hand. When spherical aberration is present, the focal plane of the marginal rays differs from that of the paraxial rays. If, in particular, as in the images of part (a) in the figures, the former is at lower z values, the knife is between the two foci, and hence the shadow for the marginal rays moves to the left hand while that for the paraxial rays is still on the right hand, thus yielding a "double-C" structure in the foucaultgram. In the case of coma, we chose the KE cutting direction in such a way to cut the right part of the comatic circle, which amounts to obscuring the contributions from the second and fourth quadrants of the beam at the

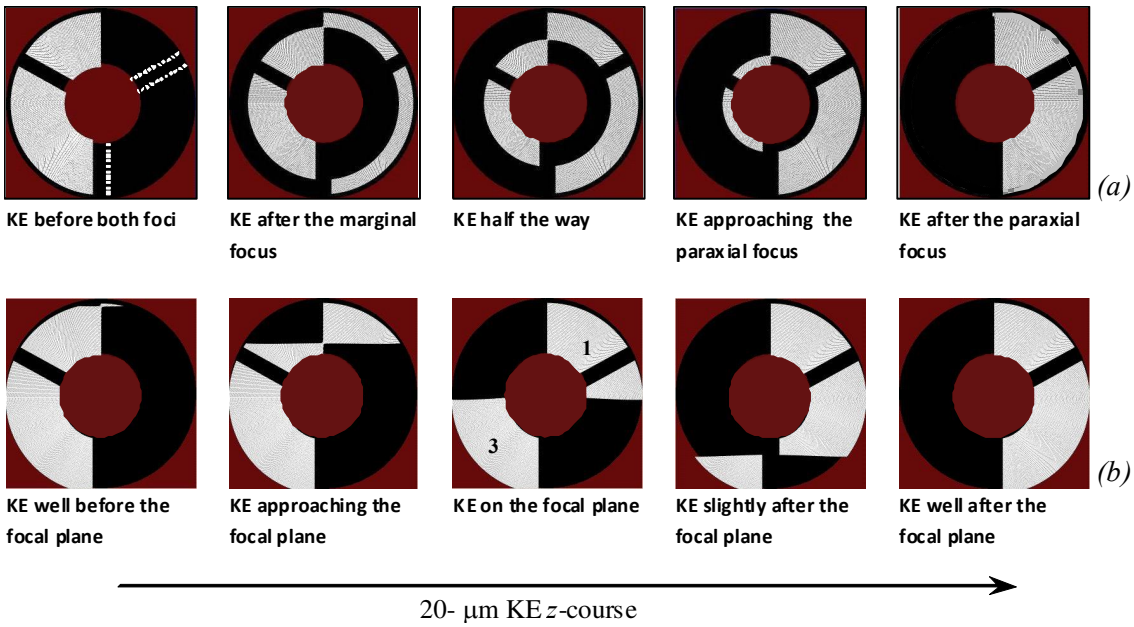

Figure 2.11: Ray-tracing calculated foucaultgrams for the ENEA MET SO in presence of *(a)* spherical aberration with the two mirrors closer to each other with respect to the concentric condition, and *(b)* coma aberration arising from a tilt of the concave mirror around an axis parallel to the x axis (see Fig. 2.9). The program simulates also the three-fins spider mount which supports the convex mirror [44].

focal plane (see the central image in Fig. 2.11b).

We can then measure the longitudinal aberration (LA) looking at the sequences like those in Fig. 2.11, defining the spherical LA as the difference between the KE z-positions corresponding to the appearance and disappearance of the double-C structure, and the coma-related LA as the difference between two symmetrical KE z-positions with respect to the focal plane corresponding to a defined change in the intensity distribution, which we fixed at the equalization of the power in the first and second quadrants and in the third and fourth quadrants, respectively, for decreasing and increasing KE z-values from the focal plane.

The modelling of the SO aberrations allows us to correct the mirror relative positions up to the SO alignment.

However, the ray-tracing program does not account for diffraction, as it is evident when comparing the foucaultgrams in Fig. 2.10 and Fig. 2.11, being the experimental images largely blurred. Because of diffraction, the estimation of the aberration amplitude becomes much more difficult or even impossible when the alignment is progressively improved and the beam dimension at the focal plane becomes comparable to λ/NA.

In order to make the ray-tracing based modelling a reliable diagnostic tool for mirror misalignments (be they externally controlled or not), diffraction is simulated in the C++ code by building, for each KE z-value, composite foucaultgrams each made up by the overlapping of single binary contributions from beams whose propagation direction is distributed around the optical axis within the $\theta = 1.22\lambda/\Phi_1$ diffraction angle (Φ_1 being the concave-mirror diameter), and whose foci are consequently spread in the focal plane within the Airy disk, that is within the diffraction limited focal spot size $1.22\lambda/NA \sim 1.6$ μm. The calculations can be effectively simplified by

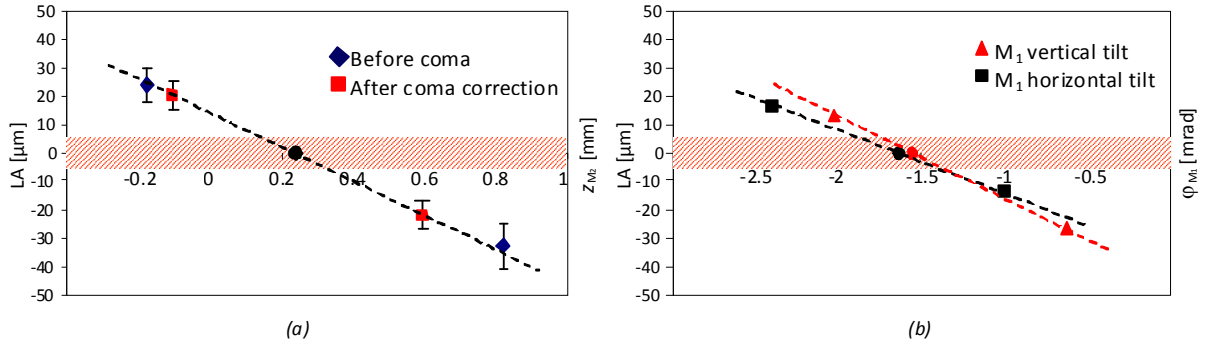

Figure 2.12: Longitudinal aberration versus SO alignment parameters: *(a)* LA vs. convex mirror M_2 z-position; *(b)* LA vs. concave mirror M_1 tilts (error bars are smaller than the symbols). In both cases, the position of the zero value on the abscissa is arbitrary. The dashed area conveys the LA range concealed by diffraction. The circles identify the values chosen as correct alignment parameters [44].

considering that this overlapping is equivalent to summing up the contributions obtainable by placing the KE at different transverse positions (for each z-value) within the Airy disk.

We measured the longitudinal aberrations, as previously defined, by varying one SO free parameter at a time. The procedure was cyclically repeated for the three degrees of freedom until the results were reproducible. The optimum position of the SO mirrors, that is the one which makes LA equal to zero for each parameter, could finally be found by means of interpolation. The results in the case of spherical aberration are reported in Fig. 2.12a, where two couples of measurements have been carried out, respectively before and after the coma correction. The improvement in the definition of the best M_2 z-position in the second run is evident looking both at the smaller error bars and at the possibility to evaluate smaller LA values. The M_1 tilt effect on LA for both orthogonal rotation axes is shown in Fig. 2.12b. In this case, the error bars are smaller due to the rather more quantitative criterium adopted to evaluate the coma-related LA.

3. ENEA MET: printing performances

As originally reported in [1], the ENEA MET, operating at 14.4 nm with a 30-μm thick Ta tape, was capable of imaging patterns from a multi-layered photomask onto a PMMA resist with edge response of 90 nm.

3.1. ENEA MET: wafer printing

The exposure was performed using a mask with Cr absorbing patterns in the form of a grating with variable period, starting from 8-μm down to 1-μm half-pitch linespace.

The fluence on the wafer can be estimated from that on the mask, taking into account the mask and SO mirror reflectivity, the SO geometrical loss and magnification. Actually, the SO transmission efficiency revealed to be definitely lower than expected, such to yield an EUV fluence of $\sim$10 μJ/cm^2/shot on the wafer plane against the expected (and needed) fluence of tens of mJ/cm^2. Therefore, we exposed the 996 000-molecular weight, 100-nm thick PMMA resist with 2000 shots, in order to reach the suitable integrated fluence of $\sim$20 mJ/cm^2. The cause of the unexpected SO deficiency has been later investigated, the relevant results being presented in the

next subsection.

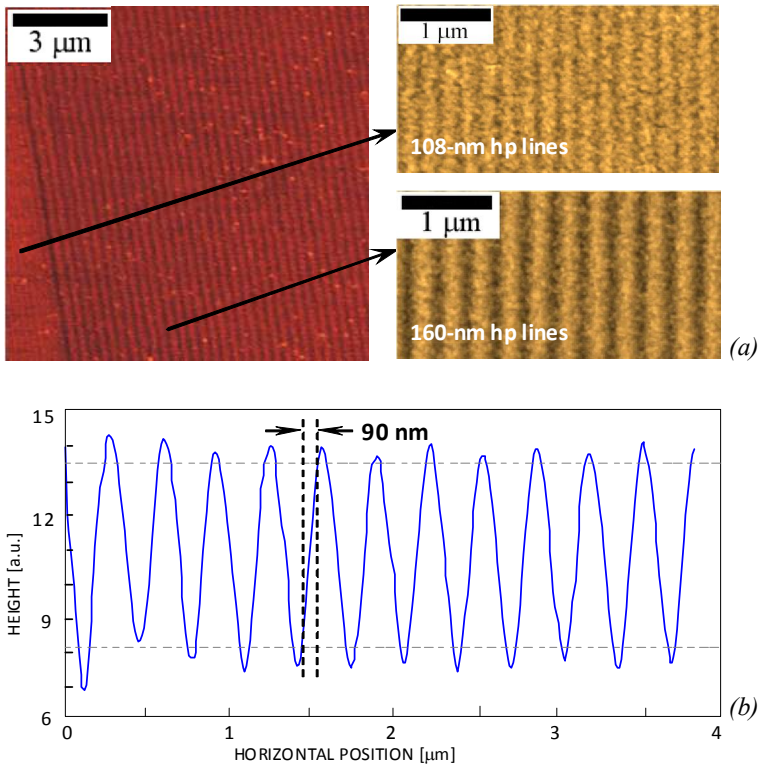

Figure 3.1: Line-space printing on PMMA: *(a)* 2D patterns of 160-nm and 108-nm half-pitch (hp) observed by an atomic force microscope. The quality of the 108-nm hp lines seems to be limited mainly by the large granularity of the photoresist. *(b)* Line profile integrated over a selected portion of the 160-nm hp line PMMA area. The horizontal dashed lines highlight the 10% and 90% modulation levels, conveying an edge response width of 90 nm.

The exposed resist was then developed by 30 s in 30% MIBK-IPA solvent, fixed in IPA and observed by an atomic force microscope. Figure 3.1 shows both the 2D image and the 1D height profile of a 160-nm half-pitch line-space pattern. The profile has been obtained by averaging height values along the lines. The measured edge response (distance to rise from 10% to 90% of the modulation depth) is 90 nm. The pattern is not printed at a full resist height, probably due to a still insufficient fluence for the used resist.

The edge response width yields a valuable estimate of the resolution of the device [45].

For an alternative, even though strictly related, estimate, we considered the PMMA modulation amplitude as a function of the spatial frequency of the imaged patterns, which should convey the modulation transfer function (MTF)[3] of the ENEA MET printing line, conforming to the

[3]We recall that the MTF is the spatial frequency response of an imaging system. It is formally given by the absolute value of the optical transfer function, which in turn follows from the 2D Fourier transform of the point spread function (or, impulse response of the imaging system) or the 1D Fourier transform of the line spread function [45, 46]. The latter is in turn the derivative (or first difference) of the edge response.

The resolution estimate, based on distinguishable line pairs (lp, i.e. a dark line next to a light line) per unit length (mm or inch), corresponds roughly to spatial frequencies at which the MTF is between 5% and 2%. An MTF of 9% is implied in the definition of the Rayleigh diffraction limit. A more reliable resolution estimate is conveyed by the spatial frequency where MTF is 50%, where the contrast has dropped by half.

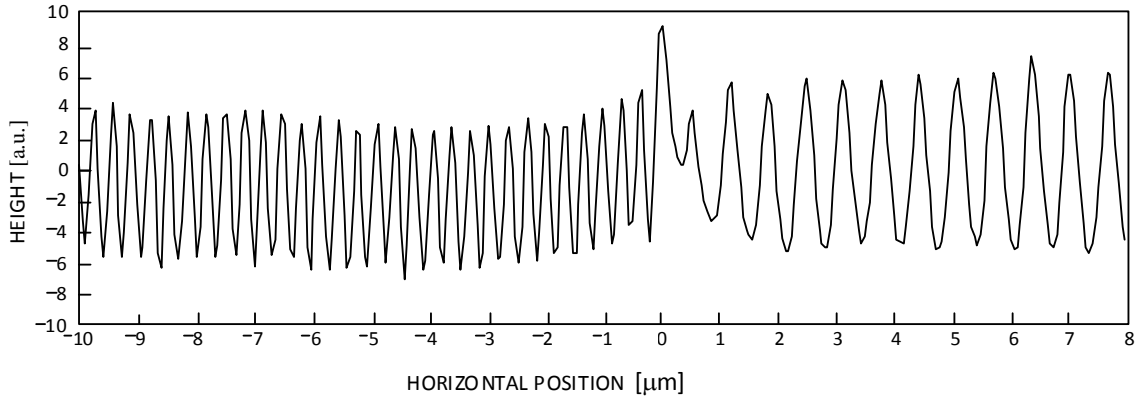

Figure 3.2: Line profile integrated over a selected portion of the PMMA area comprising contiguous regions with 320 nm (to the left) and 640 nm (to the right) full period lines.

described operation. We observed a reduction of the modulation amplitude fairly of 80% over the 320 nm patterns (Fig. 3.2), and hence at $\kappa_{80} = \frac{1}{320}$ lp/nm. Therefore, assuming for the MET imaging optics the same behaviour as a diffraction limited circular lens (see footnote 3), we may give an estimate for the printing-line optical resolution Res_{opt} according to

$$Res_{\mathsf{opt}} = \frac{0.23}{\kappa_{80}} \simeq 75 \text{ nm}.$$

Moreover, by noting that the lithographic resolution Res_{lith} is similarly ruled by the Rayleigh scaling equation [47]

$$Res_{\mathsf{lith}} = \mathrm{k}_1 \frac{\lambda}{NA},$$

where the dimensionless parameter k_1 is made by recent progresses to range as $0.3 \leq \mathrm{k}_1 \leq 0.5$, the value extent

$$32 \text{ nm} \leq Res_{\mathsf{lith}} \leq 62 \text{ nm}$$

can accordingly be estimated for the ENEA MET lithographic resolution.

We may also note that a single-shot operation was addressed to by the project [3]. Yet, as said, we were forced to operate the system for 2000 laser shots (i.e. several seconds) in order to reach a sufficient fluence to pattern the used photoresist. It is then reasonably to guess that the obtained result suffered as well from thermal and mechanical instabilities that could have been influential over the actual operation time.

For a diffraction limited circular lens, the following behaviour can empirically be drawn for the MTF as a function of the spatial frequency κ:

$$Res_{\mathsf{diff}} = \frac{1}{\kappa_{9}},$$

where Res_{diff} denotes the lens resolution according to the Rayleigh equation, $Res_{\mathsf{diff}} = 0.61\lambda/NA$ (see also Eq. (2.6)) and κ_{9} represents the spatial frequency at which, as said, the MTF is 9%. Also, MTF is 80% at a frequency κ_{80} given by $\kappa_{80} \simeq (4/17)\kappa_{9} \simeq 0.23\ \kappa_{9}$, thus implying

$$Res_{\mathsf{diff}} = \frac{0.23}{\kappa_{80}},$$

the units being in accord with those used for the spatial frequency (lp per unit length).

3.2. ENEA MET SO: checking the transmission

The reported result confirms the very good figure error of both the SO mirrors, measured to be $\leq$ 8 nm (FWHM). In contrast, as said, the SO transmission at the operating wavelength is markedly lower (roughly estimable to $\sim$ 7 times) than expected. In order to investigate the origin of this deficiency, we performed an overall SO characterization at the BEAR beam-line of ELETTRA [28], by measuring the relevant transmission over the range 13 nm $\leq \lambda \leq$ 17 nm. Technical difficulties forced us to measure the overall transmission of the objective rather than the reflectivity of each mirror, about which however reasonable conjectures can be drawn from the measured transmission, as detailed below.

The BEAR beam-line of ELETTRA is very suitable for the characterization of optics in the EUV range. It is based on a bending-magnet source and a high performance monochromator able to cover the full EUV range with an absolute accuracy of the photon energy measure of 0.1 eV, thus implying that at $\lambda = 14.4$ nm the absolute accuracy of a wavelength measurement is better than 0.02 nm.

Due to the rather small divergence of the BEAR EUV beam (1° after the last focal point), it was not convenient to place the SO at the same distance from the last focal point of BEAR as from the mask in the MET layout ($Z_o \sim 34$ cm), since this would have strongly limited the portion of the convex mirror surface illuminated by the beam. In fact, it was placed at a distance $\sim$ 124 cm from the last focal point of BEAR. This ensured that the beam cross section was larger than that of M_2, thus implying that the reflectivity measurement results from an average over the whole mirror surfaces. The consequent variation of incidence angles over the M_2-surface should produce a variation of the center wavelength of the mirror reflectivity curve, but, as a related analysis has shown, very little indeed.

The SO transmission curve $T(\lambda)$ in the EUV range, as measured at ELETTRA with an absolute accuracy of 1%, is conveyed by the blue line in Fig. 3.3a. The relevant theoretical transmission curves are also shown in the figure, as deduced on the basis of the considerations illustrated in the forthcoming subsections. The experimental curve reaches the peak value (almost 7%) at 14.8 nm rather than at 14.4 nm, and displays a bandwidth of 0.344 nm FWHM, which is smaller than the typical multilayer mirror reflectivity bandwidth ($\sim$ 6 Å FWHM and larger), and also than the observed wavelength shift. This presumably denotes a wavelength shift of both mirror reflectivities with a relative mismatch as well.

Defined by the ratio of the output to the input power, $T(\lambda)$ is related to the product of the single-mirror spatially integrated reflectivities, $\mathcal{R}_1$ and $\mathcal{R}_2$:

$$T(\lambda) = G(\lambda)\mathcal{R}_1(\lambda)\mathcal{R}_2(\lambda), \tag{3.1}$$

through the geometrical transmission factor $G(\lambda)$.

According to the measurement conditions and the characteristics of the system, the geometrical transmission factor $G(\lambda)$ arises from the concurrence of several factors. Firstly, since, as mentioned earlier, the beam cross section was larger than that of M_2, part of the incoming rays travelled externally to the mirror surface, thus amounting to an unavoidable loss of the relevant photon flux. Since the BEAR beam divergence slightly depends on the wavelength, such a loss yields a smooth dependence of G on the wavelength. Also, some of the rays hitting the convex mirror follow multiple (> 2) reflection paths before converging to the relevant best focus position, whose location on the SO axis is closer to the convex mirror than that of the rays undergoing double-reflection paths. Finally, both the rays hitting the three M_2-holding fins and those travelling almost parallel to the optical axis do not contribute to the SO imaging process.

Even though such factors, and hence $G(\lambda)$, could be estimated theoretically, we resolved to

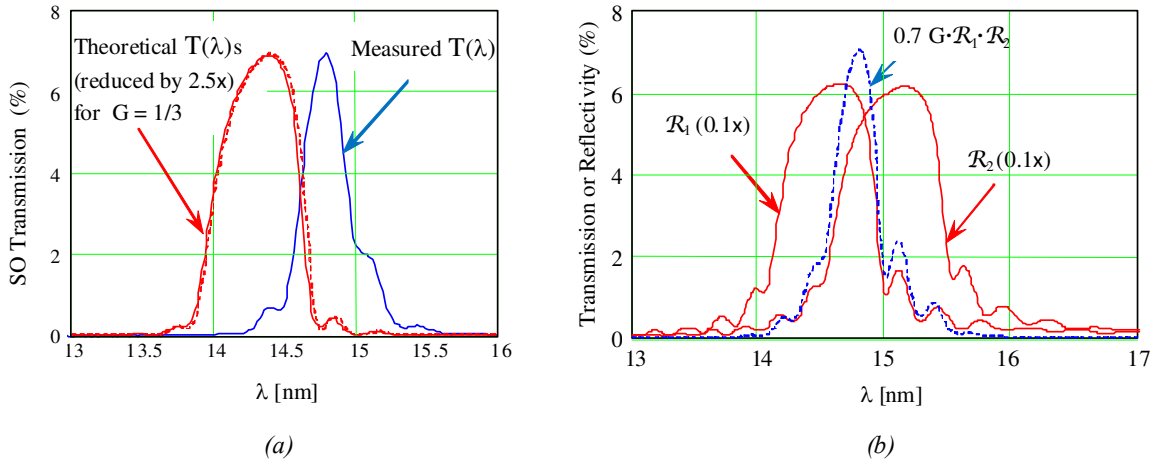

Figure 3.3: *(a)* Experimental SO transmission $T(\lambda)$ (blue line) and theoretical transmissions of an ideal SO with geometrical transmission factor $G = 1/3$, corresponding to a source located at the correct mask position (solid red line) and at approximately 90 cm farther (dashed red line). The red lines have been scaled by a factor 2.5 in order to reach the same peak value of the blue one. *(b)* Wavelength-dependent reflectivities of ideal Mo/Si multilayer mirrors centered at 14.66 nm and 15.16 nm having the same peak of 62% (red lines) and transmission of an SO resulting from such reflectivities and a geometrical transmission factor $G = 1/3$ (blue dotted line), which can be compared with the measured SO transmission (black line), also reported in panel *(a)*.

perform an experimental estimation of $G(\lambda)$ in order to obtain an estimation of the mirror reflectivity product $\mathcal{R}_1\mathcal{R}_2$ (through (3.1)) as error-free as possible. In this connection, two different procedures have been followed. One consists of assuming G be wavelength-independent so that its value could be deduced from relation (3.1) on the basis of measurements of the single-mirror reflectivities in the visible (VIS) range, carried out in our laboratory by using a doubled Nd-YAG laser at 532 nm. Accordingly, the BEAR beam has been spatially limited (by using four knifes after the monochromator) in order to select its central portion, over which the beam characteristics are fairly wavelength-independent. The other procedure consists of recording an image of the cross section of both the input and output beams (at the wavelength of the measured SO transmission-peak), which then by comparison allow us to individualize the portion of the incident beam that could not reach the SO exit.

3.2.1. SO mirror-reflectivity product as resulting from the estimate of G in the visible range

The SO transmission in the visible range (specifically, at $\lambda_{\text{green}} = 550$ nm) was measured by adjusting the BEAR line monochromator at the 0-order (no wavelength selection) and by introducing an interferential green filter (at λ_{green}) after the last focal point. As a result, we obtained $T(\lambda_{\text{green}}) = 4.0\%$. On the other hand, as said, the reflectivity of the convex mirror on its central flat part was measured (at normal incidence) in our laboratory by using a doubled Nd-YAG laser at 532 nm and resulted to be $\sim 35\%$.

Hence, by assuming $\mathcal{R}_1(\lambda_{\text{green}}) \sim \mathcal{R}_2(\lambda_{\text{green}}) \sim 35\%$, by (3.1) the SO geometrical transmission factor at 550 nm is estimated to be:

$$G_{\text{VIS}} = 1/3 = G(\lambda),$$

in accord with the value obtained from the aforementioned measurement in ENEA. As a consequence, the SO mirror-reflectivity product $\mathcal{R}_1\mathcal{R}_2$ should be three times the corresponding transmission at any wavelength, namely $\mathcal{R}_1\mathcal{R}_2 \sim 21\%$.

The transmission curve for a couple of ideal multilayer mirrors with a reflectivity peak at 14.4 nm, conforming to the estimated $G(\lambda)$, is indeed shown in Fig. 3.3a in correspondence with both a source located as in the ENEA MET (i.e. at the mask position) and as in the measurement setup (i.e. at approximately 90 cm farther), in the latter case the different incidence angles on M_2 being accounted for. The single-mirror reflectivity curves have been obtained from the Henke website [48], entering the appropriate incidence angles on the mirrors (as conveyed by specific calculations) and as multilayer periods the values measured by SESO on the samples coated during the tests for the preparation of the mirror coatings (for instance, a period of 7.48 nm on M_2 at 6 mm radially off the center).

Evidently, the SO transmission displays a reduction of both the peak value (by more than a factor 2) and the bandwidth (by a factor ~ 2) with respect to the expected values as well as an overall shift towards longer wavelengths. Such a behaviour is presumably ascribable to different wavelength shifts of the mirror reflectivities with respect to the desired value (14.4 nm), in both cases towards longer wavelengths.

In this connection, we may note that, although a small spectral shift toward longer wavelengths might be expected as a consequence of the fact that the source, as said, is not at the prescribed SO object plane, such a shift should be however much smaller than that displayed by the experimental curve, as can be inferred from a comparison between the red lines in the same figure.

For illustrative purproses, Fig. 3.3b shows the transmission of a SO (with $G = 1/3$) composed by two mirrors with reflectivies centered at $\lambda = 14.66$ nm (period of 7.557 nm) and $\lambda = 15.16$ nm (period of 7.85 nm), both having a 62% peak-value. The single-mirror reflectivities have been both reduced by a factor 10 in the plot for a better visualization of the curves. Also, the resulting SO transmission has been reduced by a factor ~ 1.4 in order to match the peak of the experimental curve (black line).

3.2.2. SO mirror-reflectivity product as resulting from the estimate of G in the EUV range

As said, the geometrical transmission factor G was also estimated in the EUV range, precisely at the wavelength of the SO transmission peak (i.e. $\lambda_{\text{peak}} = 14.8$ nm) by comparing the EUV beam spots at the SO entrance and exit, respectively recorded on a Gafchromic HD-810 Radiochromic Dosimetry film (placed at ~ 106 cm from the last focal spot of the BEAR line) and an ILFORD Q-plate film as shown in Fig. 3.4. The spot at the entrance shapes as a portion of an annulus. This is due to the deformation of the squared spot (formed by the four knifes at the monochromator exit) produced by the grazing-incidence parabolic mirror of ELETTRA, which introduces also a spatial modulation of the beam intensity, clearly visible in both images.

Such a modulation is in this case very useful since it allows to recognize in the input beam (Fig. 3.4a) the portion of the beam (highlighted by a red dashed line), which could reach the SO exit and accordingly produce on the Q-plate the same spatial modulation (similarly highlighted in Fig. 3.4b). The mesh shadow viewable in Fig. 3.4b is due to the nickel mesh of a Zr filter holder (from Luxel Incorporation) which cuts the visible light. No filters were used for the Gafchromic HD-810 film, being it not sensitive to the visible radiation. The white area external to the highlighted region of the Q-plate image corresponds to the shadow of the diverging mirror M_2 (finally surrounded by the direct beam radiation), while the small dark ring in the middle of the highlighted region corresponds to the radiation (closer to the optical axis) which, experiencing multiple-reflection paths, has then been focused along the SO axis to a plane at distance from

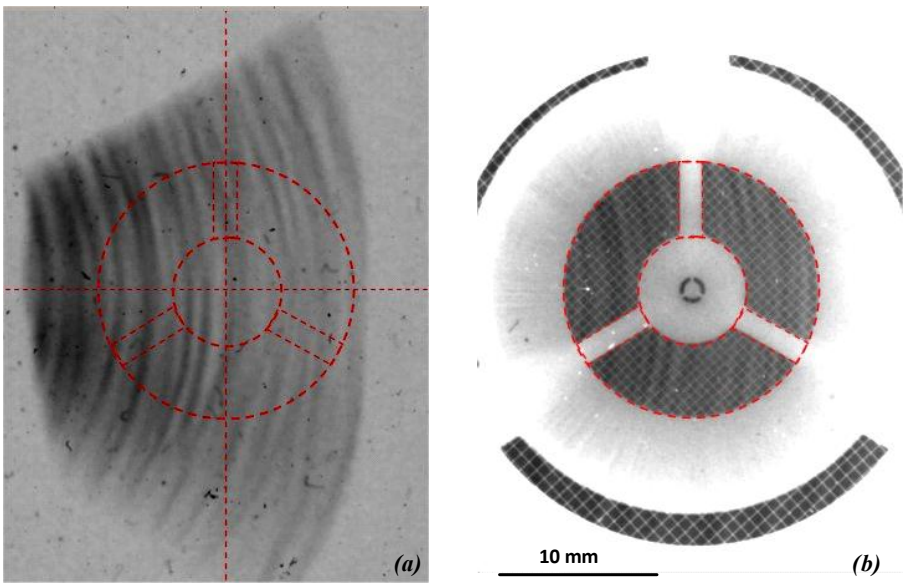

Figure 3.4: EUV spots at *(a)* the SO entrance recorded on a Gafchromic HD-810 film and *(b)* the SO exit recorded on a ILFORD Q-plate photographic plate. Both spots are at $\lambda_{peak} = 14.8$ nm.

the mirror centre of curvature shorter than the double-reflection path ray image position Z_i. The images in the figure have been acquired by a 16 bit CANON CanoScan 8400F, for which the relevant relation between the grey level g and the detected light-intensity I has been tested to be as $g(I) = I^{1/2}$.

In order to infer the radiation fluence hitting the SO, we need to know the response curve of the Gafchromic HD-810 film at the wavelength of concern. To this end, the film has been exposed at four different EUV doses at a short distance (a few centimeters) from the last focal spot of the BEAR beamline, the dose being incremented by approximately a factor two at each step (Fig. 3.5).

Limitately to the EUV doses of concern (∼32-320 J), we can fairly assume the film response to a local fluence $F(x, y)$ (i.e. the energy released on the film per unit area) be the same as that of a photographic film through the EUV range, namely [49, 50]

$$\mathcal{D}(x, y) = \mathcal{D}_S \ln(1 + \frac{F(x, y)}{F_S}),$$

where $\mathcal{D}(x, y)$ is the local film optical density, whilst $\mathcal{D}_S$ and F_S denote the EUV saturation values of the film optical density and the fluence.

Since, as earlier noted, for our scanner $g(x, y) = I(x, y)^{1/2}$, the relation between the fluence released on the film and the grey levels conveyed by the scanner can be written as

$$\log \frac{g_0}{g(x, y)} = \frac{1}{2}\mathcal{D}_S \ln(1 + \frac{F(x, y)}{F_S}),$$

g_0 being the scanner grey level for a non-exposed film ($F = 0$).

Accordingly, the fluence as a function of the image grey level can be expressed in the form

$$F(x, y) = F_S\{e^{-2\log[g(x,y)/g_0]/\mathcal{D}_S} - 1\}.$$

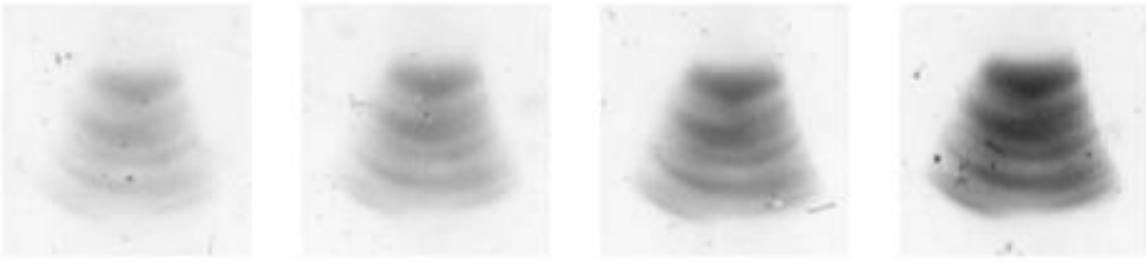

D1 D2 D3 D4

Figure 3.5: 1×1-cm^2 images of the Gafchromic HD-810 Radiochromic films exposed at the BEAR beam-line with different exposure doses: $D1 = 32.37$ J, $D2 = 63.30$ J, $D3 = 129.8$ J, and $D4 = 317.5$ J.

Finally, by integrating $F(x, y)$ on the four exposed films, the best-fit values for the two parameters F_S and $\mathcal{D}_S$ have been deduced as $F_S = 4.22$ mJ/cm^2 and $\mathcal{D}_S = 0.165$.

Then, on the basis of the above relation, the grey level map $g(x, y)$, conveyed by the image in Fig. 3.4a, yields the input fluence map $F_i(x, y)$. An additional map, say $\overline{F}_i(x, y)$, is then generated from $F_i(x, y)$, by assigning zero values to all the pixels external to the region highlighted by the red-dashed line. It is evident that $\overline{F}_i(x, y)$ represents the geometrical fraction of the input beam effectively contributing to the SO imaging.

The geometric transmission factor at the EUV wavelength, G_{EUV}, is calculated as the ratio of the integrals of $\overline{F}_i(x, y)$ and $F_i(x, y)$, thus eventually obtaining the value

$$G_{\mathsf{EUV}} = \frac{\int \overline{F}_i(x, y) dx dy}{\int F_i(x, y) dx dy} = 0.269.$$

Even though slightly lower than G_{VIS} , it increases the peak value of the SO mirror-reflectivity product (in the EUV range) to $\mathcal{R}_1\mathcal{R}_2|_{\mathsf{EUV}} = 26\%$ according to the experimental transmission peak. Also, the accuracy of this estimate is definitely higher than that based on the measurements in the visible range.

Evidently, is G_{EUV} the value of interest for the ENEA MET, the estimate of G_{VIS} and hence of $\mathcal{R}_1\mathcal{R}_2$ in the visible range representing a useful touchstone.

3.2.3. ENEA MET: SO related limitations

Due to the SO transmission center-wavelength shift with respect to the other three multilayer reflective components of the ENEA MET, the total transmission over the printing line comes to be reduced roughly by a factor six. The curves in Fig. 3.3 unambiguously shows in fact how small is the intersection between the SO transmission curve and a couple of Mo/Si mirrors working at the operating wavelength. Evidently, this limits the performance of the ENEA MET, which however might be partly recovered by replacing the aforementioned optics with optics peaked at 14.8 nm.

4. Concluding remarks

Synthesizing previous related works, the features of the ENEA EUVL MET, succesfully operated in 2008, have been reviewed. As reported in [1], exposing PMMA resist to a 14.4-nm radiation

fluence of about 20 mJ/cm^2 by means of a modified Schwarzschild objective, 160-nm half-pitch line-space patterns have been reproduced. A simple optical analysis showed that the obtained lithographic resolution is not limited by the optical quality of the projection optics, being the estimated best attainable value less than 80-nm half-pitch line-space. The MET performance is indeed limited by the SO transmission being below the design-due value, presumably as a consequence of a mirror reflectivity mismatch, as subsequent devoted analyses seem to indicate.

However, as stated in [1], the achieved results show that it is possible to attain a nanometer-scale spatial resolution using a low-cost Schwarzschild-type projection optics, as far as a proper design, figure error and alignment of the SO, and an excellent damping of both mechanical and thermal oscillations are ensured.

References

[1] S. Bollanti, P. Di Lazzaro, F. Flora, L. Mezi, D. Murra and A. Torre, First results of 160-nm-resolution patterning by laboratory-scale extreme ultraviolet projection lithography, EPL **84**, 58003 (2008)

[2] P. Di Lazzaro, S. Bollanti, F. Flora, L. Mezi, D. Murra and A. Torre, Excimer-laser-driven EUV plasma source for single-shot projection lithography, IEEE Trans. Plasma Sci., **37**, 475-480 (2009)

[3] G. Baldacchini, A. Baldesi, S. Bollanti, F. Bonfigli, G. Clementi, A. Conti, T. Dikonimos, P. Di Lazzaro, F. Flora, A. Gerardino, R. Giorgi, A. Krasilnikova, T. Letardi, N. Lisi, T. Marolo, L. Mezi, R.M. Montereali , D. Murra, E. Nichelatti, P. Nicolosi, L. Palladino, A. Patelli, M.G. Pelizzo, A. Piegari, S. Prezioso, A. Reale, V. Rigato, A. Ritucci, A. Santoni, F. Sarto, F. Scaramuzzi, E. Tefoue Kana, G. Tomassetti, A. Torre and C.E. Zheng, The Italian FIRB project on extreme ultraviolet lithography, XXVII ECLIM Conf., 6-10 September 2004, Rome, Italy.

[4] V. Bakshi (Ed.), *EUV Lithography* (SPIE and John Wiley & Sons, 2009)

[5] B. Lai, F. Cerrina and J.H. Underwood, Image formation in multilayers optics: the Schwarzschild objective, in *Applications of Thin-Film Multilayered Structures to Figured X-Ray Optics* (SPIE **563**), ed. by G.F. Marshall (SPIE, Bellingham, 1985), 174; K. Hoh and H. Tanino, Feasibility study on extreme UV/soft x-ray projection-type lithography, Bull. Electrotech. Lab. **49** (Japan), 47 (1985).

[6] H. Kinoshita, K. Kurihara, Y. Ishii and Y. Torii, Soft-x-ray reduction lithography using multilayer mirrors, J. Vac. Sci. Technol. B **7**, 1648-1651 (1989)

[7] http://www.asml.nl/asml/show.do?ctx=41905; V. Banine and R. Moors, EUV lithography and EUVL sources, 2011 Intern. Workshop on EUV and Soft X-ray Sources, Nov. 7-11, Dublin, Ireland at http://euvlitho.com/2011/2011%20Source%20Workshop%20Proceedings.pdf

[8] 2010 SEMATECH Litho Forum, New York, May 10-12, 2010. The SEMATECH Litho Forum materials can be found at http://www.sematech.org/meetings/archives.htm. See also http://www.sematech.org/corporate/annual/annual10.pdf. SEMATECH is the international consortium of leading semiconductor manufacturers.

[6] V. Bakshi (Ed.), *EUV Sources for Lithography*, vol. PM149 (SPIE Press, Bellingham, WA 2006)

[9] K. Koshelev, Current status and future of EUV and BEUV sources, 2011 Intern. Workshop on EUV and Soft X-ray Sources, Nov. 7-11, Dublin, Ireland at http://euvlitho.com/2011/2011%20Source%20Workshop%20Proceedings.pdf

[10] T. Higashiguchi, Recent Progress of Beyond EUV (BEUV) Sources, 2011 Intern. Workshop on EUV and Soft X-ray Sources, Nov. 7-11, Dublin, Ireland at http://euvlitho.com/2011/2011%20Source%20Workshop%20Proceedings.pdf

[11] F. Flora, L. Mezi, C.E. Zheng and F. Bonfigli, Krypton as stopper for ions and small debris in laser plasma sources, Europhys. Lett. **56**, 676-682 (2001)

[12] S. Bollanti, F. Bonfigli, E. Burattini, P. Di Lazzaro, F. Flora, A. Grilli, T. Letardi, N. Lisi, A. Marinai, L. Mezi, D. Murra and C. Zheng, High-efficiency clean EUV plasma source at 10-30 nm, driven by a long-pulse-width excimer laser, Appl. Phys. B **76**, 277-284 (2003)

[13] N. Kandaka and H. Kondo, Effective reduction of debris emitted from a laser-produced plasma, Jpn. J. Appl. Phys. **37**, L174-L176 (1998)

[14] J. Pankert, R. Apetz, K. Bergmann, G. Derra, M. Janssen, J. Jonkers, J. Klein, T. Kruecken, A. List, M. Loeken, C. Metzmacher, W. Neff, S. Probst, R. Prummer, O. Rosier, S. Seiwert, G. Siemons, D. Vaudrevange, D. Wagemann, A. Weber, P. Zink, O. Zitzen, Integrating Philips' extreme UV source in the alpha-tools, in *Emerging Lithographic Technologies IX* (SPIE **5751**), ed. by R. Scott Mackay (SPIE, Bellingham, 2005), 260-271

[15] C. Koay, S. George, K. Takenoshita, R. Bernath, E. Fujiwara, M. Richardson and V. Bakshi, High conversion efficiency microscopic tin-doped droplet target laser-plasma source for EUVL, in *Emerging Lithographic Technologies IX* (SPIE **5751**), ed. by R. Scott Mackay (SPIE, Bellingham, 2005), 279-292 (2005)

[16] S.S. Harilal, B. O'Shay and M.S. Tillack, Debris mitigation in a laser-produced tin plume using a magnetic field, J. Appl. Phys. **98**, 0361021-3 (2005)

[17] S.S. Harilal, B. O'Shay, Y. Tao and M.S. Tillack, Ion debris mitigation from tin plasma using ambient gas, magnetic field and combined effects, Appl. Phys. B **86**, 547-553 (2007)

[18] R. W. Coons, S. S. Harilal, D. Campos and A. Hassanein, Analysis of atomic and ion debris features of laser-produced Sn and Li plasmas, J. Appl. Phys. **108**, 063306 (2010)

[19] D. Campos, S. S. Harilal and A. Hassanein, The effect of laser wavelength on emission and particle dynamics of Sn plasma, J. Appl. Phys. **108**, 113305 (2010)

[20] S. Bollanti, P. Di Lazzaro, F. Flora, T. Letardi, A. Marinai, A. Nottola, K. Vigli-Papadaki, A. Vitali, F. Bonfigli, N. Lisi, L. Palladino, A. Reale and C. E. Zheng, Toward a high-average-power and debris-free soft x-ray source for microlithography pumped by a long-pulse excimer laser, in *EUV, X-Ray, and Neutron Optics and Sources* (SPIE **3767**), ed. by C. A. MacDonald, K. A. Goldberg, J. R. Maldonado, H. H. Chen-Mayer, S. P. Vernon (SPIE, Bellingham, 2003), 33-44

[21] http://www.frascati.enea.it/fis/lac/excimer/egeria.html

[22] S. Bollanti, D. Amodio, A. Conti, P. Di Lazzaro, F. Flora, L. Mezi, D. Murra, A. Torre, C. E. Zheng, D. Garoli, M.G. Pelizzo, P. Nicolosi, V. Mattarello, V. Rigato, A. Gerardino, Progress report on a 14.4 nm Micro-Exposure Tool based on a laser-produced-plasma: debris mitigation system results and other issues, in *Ultrafast X-Ray Sources and Detectors* (SPIE. 6703), ed. by Z. Chang, G. A. Kyrala, J.-C. Kieffer (SPIE, Bellingham, 2007), 670308

[23] P. Di Lazzaro, S. Bollanti, F. Flora, L. Mezi, D. Murra and A. Torre, Characterisation of sources for Extreme UltraViolet Lithography: measurement of ion and particulate emission, and suppression mechanisms, this volume

[24] S. Bollanti, P. Di Lazzaro, F. Flora, L. Mezi, D. Murra and A. Torre, Laser-plasma-source debris-related investigations: an aspect of the ENEA micro-exposure tool, Appl. Phys. B **96**, 479-490 (2009)

[25] http://www.mathworks.com/products/matlab/

[26] http://www.medialario.com

[27] http://www.lnl.infn.it

[28] http://www.elettra.trieste.it/experiments/beamlines/bear/index.html

[29] http://www.inf.cnr.it

[30] K. Schwarzschild, Untersuchugen zur geometrischen Optik, Abh. WIss. Goett. Math. Phys. K1 NF 4, 1-3 (1905)

[31] http://www.seso.com

[32] A. Budano, F. Flora, L. Mezi, Analytical design method for a modified Schwarzschild optics, Appl. Opt. **45**, 4254-4263 (2006)

[33] I.G. Artyoukov and K.M. Krymski, Schwarzschild objective for soft-X rays, Opt. Eng. **39**, 2163-2170 (2000)

[34] S. Bollanti, P. Di Lazzaro, F. Flora, L. Mezi, D. Murra and A. Torre, Conventional and modified Schwarzschild objective for EUV lithography: design relations, Appl. Phys. B **85**, 603 (2006)

[35] S. Bollanti, P. Di Lazzaro, F. Flora, L. Mezi, D. Murra and A. Torre, Further comparisons between the conventional and the modified Schwarzschild objectives, Appl. Phys. B **91**, 127 (2008)

[36] Information on and a demonstration version of the ZEMAX package are in www.optima-research.com

[37] S. Bollanti, P. Di Lazzaro, F. Flora, L. Mezi, D. Murra and A. Torre, Mask tilt effects counteracted by wafer tilt in an SO-based EUV lithography setup, in *Optical Design and Engineering II* (SPIE **5962**), ed. by L. Mazuray, R. Wartmann (SPIE, Bellingham, 2005), 5962Y-1

[38] T. Scheimpflug, Der photoperspektrograph und seine anwendung, Photogr. Korr. **43**, 516-531 (1906)

[39] M. L. Foucault, Description des procédés employés pour reconnaître la configuration des surfaces optiques, C. R. Acad. Sci. Paris **47**, 958 (1858)

[40] R. B. Korsmeyer, Foucault test for a Schwarzschild, Sky & Telescope **3**, 18 (1944)

[41] A.K. Ray-Chaudhuri, W. Ng, S. Liang, S. Singh, J. T. Welnak, J. P. Wallace, C. Capasso, F. Cerrina, G. Margaritondo, J. H. Underwood, J. B. Kortright, and R. C. C. Perera, First results of microspectroscopy from a scanning photoemission microscope with a submicron probe size, J. Vac. Sci. Technol. A **11**, 2324-2329 (1993)

[42] A.K. Ray-Chaudhuri, W. Ng, S. Liang and F. Cerrina, Soft X-ray Foucault test: a path to diffraction-limited imaging, Nucl. Instr. & Meth. A **347**, 364-371 (1994)

[43] F. Barbo, M. Bertolo, A. Bianco, G. Cautero, S. Fontana, T. K. Johal, S. La Rosa, G. Margaritondo and K. Kaznacheyev, Spectromicroscopy beamline at ELETTRA: Performances achieved at the end of commissioning, Rev. Sci. Instrum. **71**, 5-10 (2000)

[44] S. Bollanti, P. Di Lazzaro, F. Flora, L. Mezi, D. Murra and A. Torre, New technique for aberration diagnostics and alignment of an extreme ultraviolet Schwarzschild objective, Proc. 2nd Int. Conf. Frontiers in Diagnostic Technologies, Frascati, 28-30 November 2011, submitted for publication in a special volume of Nucl. Instr. & Meth. A

[45] S.W. Smith, *The Scientist and Engineer's Guide to Digital Signal Processing* (California Techn. Pub, 1997), Ch. 25; http://www.dspguide.com/pdfbook.htm

[46] J.D. Gaskill, *Linear systems, Fourier transforms, and optics* (Wiley & Sons, New York,1978)

[47] B. J. Lin, Where is the lost resolution, in *Optical Microlithography V* (SPIE **633**), ed. by H.L. Stover (SPIE, Bellingham, 1986), 44

[48] http://henke.lbl.gov/optical constants/

[49] B. L. Henke, S. L. Kwok, J. Y. Uejio, H. T. Yamada, and G. C. Young, Low-energy x-ray response of photographic films. I. Mathematical models, JOSA B **1**, 818-827 (1984)

[50] G.J. Tallents, J. Krishnan, L. Dwivedi, D. Neely, I.C.E. Turcu, Film calibration for soft X-ray wavelength, in *Applications of X rays generated from lasers and other bright sources* (SPIE **3157**), ed. by G.A. Kyrala, J.-C. J. Gauthier (SPIE, Bellingham, 1997), 281-290